Journal of Materials Chemistry A

ROYAL SOCIETY OF CHEMISTRY

PAPER

View Article Online
View Journal

Cite this: DOI: 10.1039/d5ta03374h

Physics-guided machine learning of excited-state properties for the design of high-performance TADF emitters

Sanyam, † Bibhas Das † and Anirban Mondal *

The rational design of thermally activated delayed fluorescence (TADF) and inverted singlet–triplet (INVEST) emitters demands accurate prediction of critical photophysical properties, particularly singlet–triplet energy gaps (ΔE_{ST}) and oscillator strengths (f). Conventional machine learning (ML) models often neglect the underlying physics, limiting their transferability and interpretability across chemical space. In this work, we develop a physics-informed machine learning (PIML) framework that leverages physically meaningful molecular descriptors to predict ΔE_{ST} and f with high accuracy and robust generalization. Training on a chemically diverse dataset of over 39 000 compounds, our models achieve correlation coefficients (r) between 0.77 and 0.88 and mean absolute errors (MAE) below 0.1 eV for ΔE_{ST} and 0.02 for f on unseen test data. The reliability of the PIML models is further validated *via* leave-one-out cross-validation and external datasets, including 28 experimentally reported emitters, for which our model outperforms state-of-the-art quantum chemical and ML approaches. Beyond predictive accuracy, integrating interpretability tools reveals the exchange integral, dynamic spin polarization, and excited-state energies as dominant factors controlling the target properties—offering mechanistic insights often inaccessible in standard black-box models. Finally, leveraging the predictive power of the trained models, we performed high-throughput screening of 400 newly designed TADF emitters, successfully identifying promising candidates with optimal ΔE_{ST} and f combinations for OLED applications. This study highlights the strength of combining physical intuition with data-driven modeling, offering an efficient, scalable, and interpretable route for accelerating the discovery of next-generation optoelectronic materials.

Received 28th April 2025
Accepted 22nd August 2025

DOI: 10.1039/d5ta03374h

rsc.li/materials-a

1 Introduction

Organic light-emitting diodes (OLEDs) rely on efficient emitter materials, which are crucial in determining device performance.[1–8] Conventional fluorescent emitters suffer from limited internal quantum efficiency (IQE) due to the restriction of radiative recombination to singlet excitons.[9–14] In contrast, phosphorescent materials[15–18] achieve near-unity IQE by harnessing both singlet and triplet excitons. However, the prolonged triplet-state lifetime in phosphorescent materials leads to efficiency roll-off and long-term stability issues. To overcome these challenges, alternative emissive mechanisms such as thermally activated delayed fluorescence (TADF)[1–3,19,20] and inverted singlet–triplet (INVEST) emission[21–24] have emerged. These mechanisms exploit reverse intersystem crossing (RISC) enabled by small singlet–triplet energy gaps (ΔE_{ST}), facilitating efficient radiative decay. However, minimizing ΔE_{ST} often results in a spatially separated highest occupied molecular orbital (HOMO) and lowest unoccupied molecular orbital (LUMO), which in turn reduces the oscillator strength (f) and lowers emission efficiency.[3–8] This trade-off between ΔE_{ST} and f is a fundamental challenge in designing next-generation OLED emitters, necessitating a deeper understanding of electronic structure–property relationships.

Computational chemistry plays a pivotal role in the discovery of OLED materials.[25–29] Density functional theory (DFT) methods are widely used for electronic structure calculations but often fail to describe charge-transfer excitations and double-excitation contributions accurately.[30–32] Higher-level methods, such as second-order algebraic diagrammatic construction [ADC(2)] and coupled-cluster approaches, provide reliable ΔE_{ST} predictions[33] but are computationally prohibitive for large-scale screening.[26] Machine learning (ML) offers a promising alternative, enabling rapid property predictions based on molecular descriptors.[27–29,34,35] However, conventional ML models—such as random forest, gradient boosting, and neural networks—often act as black-box predictors, lacking physical interpretability.[29,36,37] This limits their utility in understanding the microscopic origins of emitter performance and makes it difficult to extract meaningful design principles.

To address these limitations, physics-informed machine learning (PIML) integrates fundamental physical insights into

Department of Chemistry, Indian Institute of Technology Gandhinagar, Gujarat, 382355, India. E-mail: amondal@iitgn.ac.in

† Sanyam and Bibhas Das contributed equally to this work.

predictive models, ensuring physically consistent and interpretable results. In this work, we develop a physics-inspired machine learning model to predict both ΔE_{ST} and f in TADF and INVEST emitters. Our model incorporates domain knowledge by leveraging the Sure-Independence Screening and Sparsifying Operator (SISSO) framework[38,39] to identify low-dimensional physically meaningful descriptors derived from the semi-empirical Pariser–Parr–Pople (PPP) method.[40–42] The novelty of our approach lies in combining semi-empirical quantum chemical methods with PIML to achieve prediction accuracy comparable to high-level configuration interaction singles and doubles [CIS(D)/cc-pvDZ] method calculations at a fraction of the computational cost. Moreover, our method provides physical interpretability by linking the target properties directly to fundamental molecular descriptors such as exchange integrals (K), HOMO–LUMO overlap (S), and dynamic spin polarization (DSP, P). The same set of descriptors is used to model both ΔE_{ST} and f, reflecting the common physical origin of these two quantities.

Our model was trained on a dataset of approximately 39 000 TADF and INVEST emitters, achieving correlation coefficients (r) between 0.77 and 0.88 for both ΔE_{ST} and f predictions, with mean absolute errors (MAE) below 0.1 eV for ΔE_{ST} and 0.02 for f on the test set. The robustness of the model was validated using leave-one-out cross-validation (LOOCV) and external dataset testing, demonstrating consistent predictive performance. Additionally, applying the model to an experimental dataset of 28 emitters with reported singlet–triplet gaps yielded a root mean square error (RMSE) of 0.054 eV, MAE of 0.046 eV, and maximum absolute error (MaxAE) of 0.086 eV—significantly outperforming previous high-level quantum mechanical methods[33,43] and machine learning models.[44–46] These results demonstrate that our physics-inspired model not only enhances predictive accuracy but also reduces computational costs, making it suitable for large-scale screening. The practical utility of this framework was further exemplified through high-throughput screening of 400 newly designed emitters, which successfully identified a subset of candidates with optimal combinations of ΔE_{ST} and oscillator strength for high-efficiency OLED applications. To gain deeper insights, we employed SHapley Additive exPlanations (SHAP), joint distribution plots, and multivariate analysis, which consistently highlighted the exchange integral as the primary factor governing both ΔE_{ST} and oscillator strength—a key feature often underrepresented in conventional ML models.[44–46] By leveraging a semi-empirical dataset with computational costs several orders of magnitude lower than high-level *ab initio* methods, our approach achieves prediction accuracies comparable to CIS(D). This scalable, interpretable framework bridges the gap between computational efficiency and predictive accuracy, offering a practical and physically grounded platform for next-generation OLED emitter discovery.

2 Computational details

The computational workflow, depicted in Fig. 1, outlines a systematic approach for selecting and screening key descriptors that govern the target properties ΔE_{ST} and f. These descriptors include singlet (E_{S_1}) and triplet (E_{T_1}) energies, HOMO–LUMO overlap (S), exchange integral (K), and dynamic spin polarization (P), which capture the underlying physics of TADF and INVEST emitters. The target values, ΔE_{ST} and f, were derived from a benchmark dataset by Pollice *et al.*,[26] originally computed using configuration interaction singles and doubles [CIS(D)]. To balance computational efficiency with molecular diversity, we curated a representative subset comprising 39 192 compounds for ΔE_{ST} (Dataset-I) and 31 234 compounds for f (Dataset-II) for model training and testing. The selected dataset encompasses both $4n\pi$ (anti-aromatic) and $(4n + 2)\pi$ (aromatic) electron systems, with ring sizes ranging from four to fourteen members and including various fused-ring architectures. Nitrogen is the predominant heteroatom in these structures, reflecting common design motifs in TADF and INVEST emitters. The dataset-I identified 21 882 compounds (55.8%) as conventional TADF molecules, while the remaining 17 310 compounds (44.2%) were classified as INVEST emitters. This comprehensive molecular representation ensures that the dataset captures both typical and inverted singlet–triplet gap systems, thereby enhancing the generalizability of the resulting machine-learning models.

2.1 Data set compilation: Pariser–Parr–Pople descriptors

Ground-state geometries and excited-state properties, including the singlet–triplet energy gap, oscillator strength, and molecular structures, were sourced from ref. 26. These optimized geometries served as input for computing key descriptors using the Pariser–Parr–Pople model.[40–42] The distribution of PPP-derived descriptors—E_{S_1}, E_{T_1}, K, P, and S—is illustrated in Fig. 2. The singlet and triplet excitation energies (E_{S_1} and E_{T_1}) are observed up to approximately 0.15 eV and 0.1 eV, respectively. Both distributions exhibit distinct features with multiple localized maxima rather than a smooth unimodal trend (Fig. 2a and b). The exchange integral (K) is concentrated between 0.0 and 0.04 eV, with an asymmetric distribution skewed towards lower values (Fig. 2c). The distribution of P spans from approximately −0.01 eV to 0.005 eV, exhibiting multiple peaks (Fig. 2d). The HOMO–LUMO overlap (S) varies broadly from 0.3 to 1.0 eV, forming a right-skewed distribution with a predominant peak around 0.7 (Fig. 2e).

2.2 Data set compilation: target properties

We also analyzed the distribution of target properties—oscillator strength and singlet–triplet energy gap. The ΔE_{ST} values range from −0.68 to 0.80 eV (Fig. 2f). In contrast, the oscillator strength values predominantly fall within 0.0003 to 0.45, exhibiting a skewed distribution with a peak at lower values (Fig. 2g). Statistical analysis further supports this trend: the mean and median for ΔE_{ST} are 0.081 and 0.122 eV, while for f, they are 0.053 and 0.038, respectively. The standard deviations for ΔE_{ST} (0.309 eV) and f (0.048) indicate moderate variability within the dataset. The combination of these distribution characteristics ensures a well-structured dataset, facilitating ML

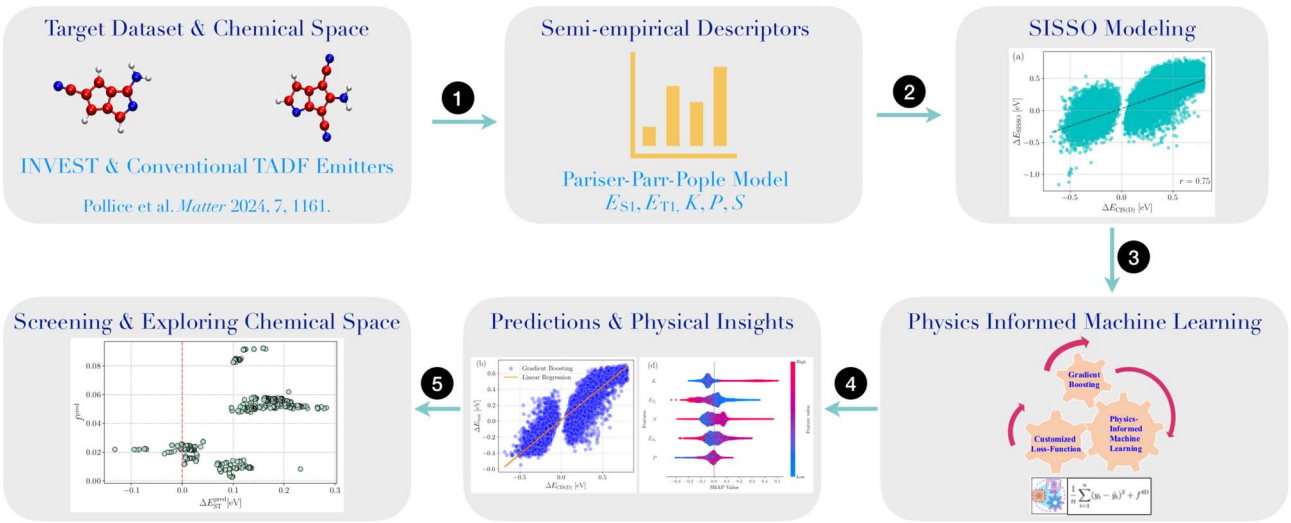

Fig. 1 Schematic overview of the computational framework adopted in this work.

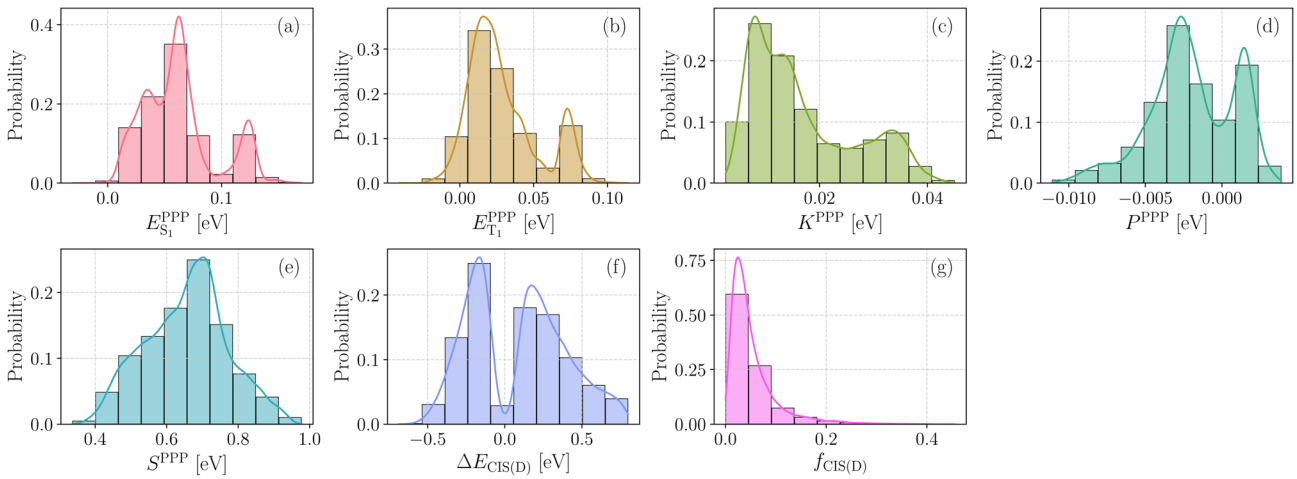

Fig. 2 Distribution of the absolute values of various properties. Panels (a)–(e) display the descriptors, including the singlet (E_{S_1}) and triplet (E_{T_1}) energies, exchange integral (K), dynamic spin polarization (P), and the HOMO–LUMO overlap (S), all derived using the Pariser–Parr–Pople semi-empirical method.[40–42] Panels (f) and (g) illustrate the target quantities, including the singlet–triplet energy gap (ΔE_{ST}) and oscillator strength (f), which were obtained using CIS(D)/cc-pvDZ level of theory, as reported in ref. 26.

model training and improving the predictive accuracy and robustness of the framework.

2.3 SISSO-based modeling

To establish data-driven relationships between the PPP descriptors and the target properties, we employed the SISSO++ algorithm.[38,39] This method is particularly valuable for identifying explicit functional forms that connect descriptors to target quantities. SISSO formulates the predictive model as $y = f(\Phi)$, where $\Phi = [\phi_1, \phi_2, \ldots, \phi_n]$ represents the essential descriptors, and y denotes the target property to be predicted. Given a dataset of N training samples, the algorithm assumes that y can be approximated as a combination of simple mathematical functions applied to primary descriptors. To construct these functions, SISSO recursively employs fundamental operations such as addition, subtraction, multiplication, and division alongside more complex transformations, including absolute values, exponentials, logarithms, squaring, cubing, square and cube roots, and trigonometric functions. At each iteration, SISSO selects the most relevant feature transformations by maximizing their correlation with the target property or residuals from the previous step. This iterative refinement ensures that the model progressively captures essential nonlinear dependencies. The final model is constructed as an optimal linear combination of selected nonlinear transformations. To prevent overfitting, model complexity is regulated using ℓ_0-regularization, which ensures sparsity by limiting the number of active features.

The model's predictive performance was assessed using standard error metrics, including RMSE, maximum absolute

error, and Pearson correlation coefficient. The RMSE was defined as

$$\mathrm{RMSE} = \sqrt{\frac{1}{N}\sum_{i=1}^{N}(y_i - \hat{y}_i)^2}, \quad (1)$$

where y_i and $\hat{y}_i$ are the actual and predicted values for the i-th sample, respectively. Although models with up to five dimensions were initially explored, we adopted a 4D model (f^{4D}), balancing accuracy and computational efficiency. The resulting equations directly relate PPP descriptors to ΔE_{ST} and f, providing a transparent and interpretable framework for predicting emitter properties.

2.4 Physics informed machine learning

Building on the SISSO-derived 4D equations, we developed a physics-informed machine learning framework that integrates symbolic physical relations directly into a customized gradient boosting regressor. The SISSO-derived 4D expression, including its coefficients, is embedded in the loss function to enforce physically meaningful constraints and improve generalizability. The total loss combines the traditional Mean Squared Error (MSE) with a physics-based penalty term:

$$\text{Loss function} = \frac{1}{n}\sum_{i=1}^{n}(y_i - \hat{y}_i)^2 + f^{4D} \quad (2)$$

where n is the number of samples, y_i and $\hat{y}_i$ denote the actual and predicted values, and f^{4D} encodes the SISSO-derived expression. This formulation guides the model to balance data-driven predictions with quantum-mechanical constraints.

The model was trained on 80% of the dataset and validated on the remaining 20%. The input descriptors—E_{S_1}, E_{T_1}, K, P, and S—were independently standardized to preserve physical interpretability. Hyperparameter optimization was performed using Optuna's Tree-structured Parzen Estimator (TPE) algorithm, maximizing the Pearson correlation on the validation set.[47] Model training includes complete reproducibility *via* logging, seed control, and configuration files. All code and data are publicly available *via* GitHub. A comprehensive PIML architecture with schematic overview and workflow is presented in Section S1, Fig. S1 and S2 of the SI.

3 Results and discussion

The distribution of the target and dependent variables, previously described in the methodology section, provides the foundation for our model development. To predict ΔE_{ST}, we designed three distinct models: one for positive ΔE_{ST} values, negative ΔE_{ST} values, and a third for the entire ΔE_{ST} range. This stratified approach aims to explore whether the selected descriptors exert differential influence on positive and negative ΔE_{ST} values, thereby enhancing interpretability. In contrast, for oscillator strength and the full ΔE_{ST} range, we developed single, unified models using the entire dataset to capture broader trends and dependencies. The subsequent sections present a detailed evaluation of each model, offering insights into their predictive performance, interpretability, and underlying physical implications.

3.1 Emitters with positive S_1–T_1 gap (ΔE_{ST}^{+})

We initiated our calculations with SISSO modeling, exploring dimensionalities ranging from one to five. Upon comparing the models, we observed that the four-dimensional (4D) and five-dimensional (5D) models exhibited nearly identical accuracy. However, the 4D model was computationally more efficient while maintaining comparable predictive performance. Therefore, we focused our analysis on models between one and four dimensions. Notably, as the dimensionality increased, the complexity of the resulting equations also grew. This increase in complexity, however, was accompanied by a marked improvement in Pearson correlation, along with a substantial reduction in the maxAE and RMSE. These trends emphasize the importance of balancing computational cost and prediction accuracy when selecting the optimal model. Performance metrics for the 1D, 2D, and 3D models are summarized in Table S1, while the performance of the 4D model is detailed in Table 1. For the positive ΔE_{ST} values, the 4D model achieved an RMSE of 0.108 eV, a maxAE of 0.508 eV, and a Pearson correlation coefficient (r) of 0.809. The corresponding equation, which relates the target quantities to the selected descriptors and their coefficients, is also presented in Table 1. Additionally, Fig. 3a shows the SISSO model's predictive performance for ΔE_{ST}^{+}, illustrating the reasonably strong correlation between the predicted and actual values.

Despite these promising results, the relatively high RMSE and maxAE suggest room for further refinement. To improve predictive accuracy, we integrated the SISSO-derived equation (see Table 1) as an additional loss function within a PIML framework based on a custom gradient boosting algorithm. This hybrid approach aimed to leverage both the simplicity of analytical descriptor-based modeling and the flexibility of machine learning to capture complex nonlinear relationships. The performance of the PIML model, tested on an unseen dataset, is shown in Fig. 3b. Remarkably, the PIML model achieved a correlation coefficient (r) of 0.86, surpassing the direct SISSO model (Fig. 3a). Furthermore, the mean absolute error (MAE) and RMSE were 0.07 eV and 0.09 eV, respectively, indicating a substantial enhancement in predictive accuracy. The corresponding training correlation plot is provided in Fig. S3, and the detailed metrics are summarized in Table 2.

To further validate the robustness of the PIML model, we employed leave-one-out cross-validation. LOOCV is a rigorous evaluation method wherein each data point is iteratively designated as the test set while the model is trained on the remaining data points. For a dataset containing N data points, this process involves training the model N times, using $N - 1$ data points for training and the remaining one for validation. This approach ensures that every data point contributes to the validation process, thus providing an unbiased assessment of the model's performance. The LOOCV results confirm the robustness of the PIML model, yielding a correlation coefficient

Table 1 SISSO fourth-dimensional (f^{4D}) model parameters for singlet–triplet properties: ΔE_{ST}^{+}, ΔE_{ST}^{-}, ΔE_{ST}, and f. Listed are the descriptor coefficients (c_0, a_0, a_1, a_2, a_3) along with the model performance metrics: RMSE, MaxAE, and correlation coefficient (r)

Model (f^{4D})	c_0	a_0	a_1	a_2	a_3	RMSE	MaxAE	r
$\Delta E_{ST}^{+} = c_0 + a_0(\sqrt[3]{E_{T_1}} \times \ln S) + a_1 \times (S^6 \times S \times P) + a_2 \times (\lvert(P \times K) - K^3\rvert) + a_3 \times (K/S)^3$	2.909×10^{-1}	4.739×10^{-1}	-1.350×10^{2}	-2.067×10^{3}	3.204×10^{3}	0.108	0.508	0.809
$\Delta E_{ST}^{-} = c_0 + a_0(S^2/\lvert P - K\rvert) + a_1 \times ((P/K)/\lvert P - K\rvert) + a_2 \times ((K/S) \times P \times K) + a_3 \times (\exp(E_{T_1}) - \lvert P - K\rvert)$	-7.816×10^{0}	1.139×10^{-3}	-2.865×10^{4}	-2.253×10^{0}	2.138×10^{0}	0.076	0.393	0.665
$\Delta E_{ST} = c_0 + a_0({E_{T_1}}^3 \times S \times P) + a_1 \times (S^6/K^2) + a_2 \times (\lvert\sqrt[3]{E_{T_1}} - (S - E_{T_1})\rvert) + a_3 \times (K^3 \times \ln S)$	-2.396×10^{-1}	1.918×10^{5}	7.829×10^{-5}	4.598×10^{-1}	-4.059×10^{4}	0.207	1.088	0.747
$f = c_0 + a_0(\exp(-(S/K))) + a_1 \times ((K/S) \times \lvert P\rvert) + a_2 \times (\lvert K - E_{T_1}\rvert - (S \times E_{T_1})) + a_3 \times (K^2 \times \ln S)$	2.310×10^{-2}	-1.680×10^{7}	-2.231×10^{2}	1.096×10^{0}	-3.368×10^{2}	0.034	0.341	0.714

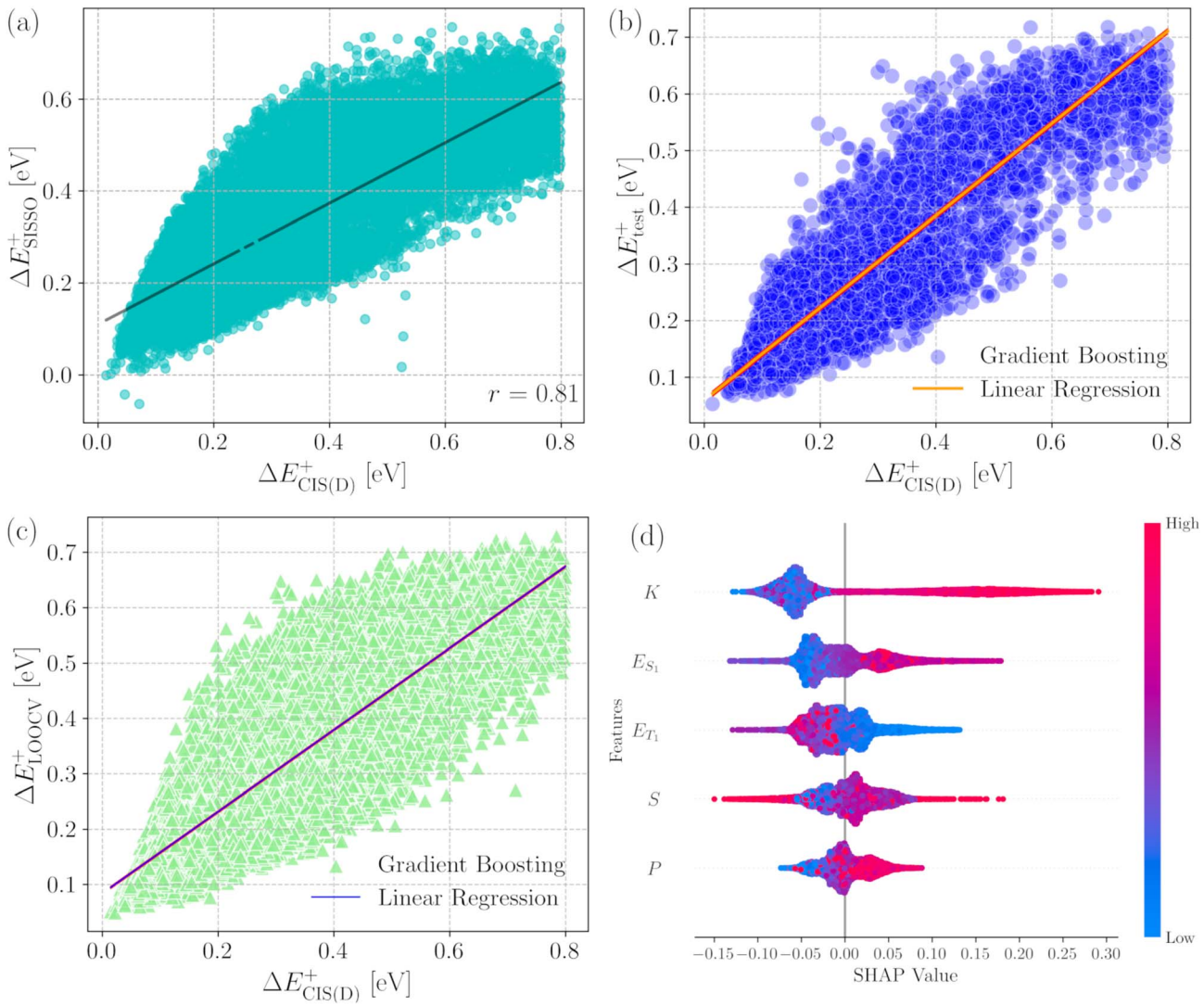

Fig. 3 Model evaluation and interpretability analysis for ΔE_{ST}^{+} prediction: (a) SISSO model performance, (b) PIML model performance on the testing dataset, (c) leave-one-out cross-validation results for model robustness assessment, and (d) SHAP analysis illustrating the feature contributions to ΔE_{ST}^{+} predictions.

Table 2 Performance metrics for PIML predictions: the table summarizes the correlation coefficient (r), mean absolute error (MAE), and root mean squared error (RMSE) across three validation methods—test set performance ($PIML^{test}$), training set performance ($PIML^{train}$), and Leave-One-Out Cross-Validation (LOOCV)

Target property	Metrics	$PIML^{test}$	$PIML^{train}$	LOOCV
ΔE_{ST}^{+}	r	0.86	0.93	0.86
	MAE	0.07	0.05	0.07
	RMSE	0.09	0.06	0.09
ΔE_{ST}^{-}	r	0.77	0.87	0.77
	MAE	0.05	0.04	0.05
	RMSE	0.06	0.05	0.06
ΔE_{ST}	r	0.88	0.95	0.88
	MAE	0.11	0.08	0.11
	RMSE	0.14	0.10	0.14
f	r	0.84	0.93	0.84
	MAE	0.02	0.01	0.02
	RMSE	0.03	0.01	0.03

of 0.86, consistent with the testing results (Fig. 3c). Additionally, the MAE and RMSE values remained at 0.07 eV and 0.09 eV, respectively (see Table 2), below the 0.1 eV benchmark. These findings reinforce the reliability and predictive accuracy of the PIML model, underscoring its ability to capture the underlying physical trends governing ΔE_{ST}^{+}. This strong performance demonstrates the effectiveness of combining descriptor-based SISSO modeling with ML techniques to improve predictive accuracy while maintaining interpretability.

We performed SHAP analysis alongside additional multivariate techniques to further interpret the PIML model and understand the underlying physics driving the prediction of positive singlet–triplet energy gaps (ΔE_{ST}^{+}). These analyses aim to quantify individual descriptors' relative contributions and interactions, offering a detailed understanding of the model's internal logic and alignment with physical principles. The SHAP summary plot (Fig. 3d) reveals a distinct hierarchy among the five descriptors, highlighting their roles in influencing the predicted energy gaps. The exchange integral (K) stands out as the most influential descriptor. High values of K (denoted in red) consistently lead to substantial positive SHAP values. This observation aligns with fundamental quantum mechanical intuition—K quantifies the energy associated with electron exchange and is directly related to the energetic cost of promoting an electron from a singlet to a triplet state. Interestingly, the SHAP distribution for K is strongly skewed, with positive contributions far outweighing negative ones, underscoring its unidirectional and dominant impact on increasing ΔE_{ST}^{+}. In contrast, the singlet energy shows a more intricate pattern, with high and low values producing mixed SHAP effects. This suggests that E_{S_1}'s impact on ΔE_{ST}^{+} is context-dependent, potentially interacting with other variables non-linearly. The triplet energy, however, exhibits a more predictable inverse relationship: higher E_{T_1} values generally correspond to negative SHAP contributions, reflecting the physical expectation that raising the triplet energy compresses the singlet–triplet gap. The overlap integral (S) and dynamic spin polarization (P) show more balanced SHAP distributions around zero but tend to contribute positively, especially for higher values.

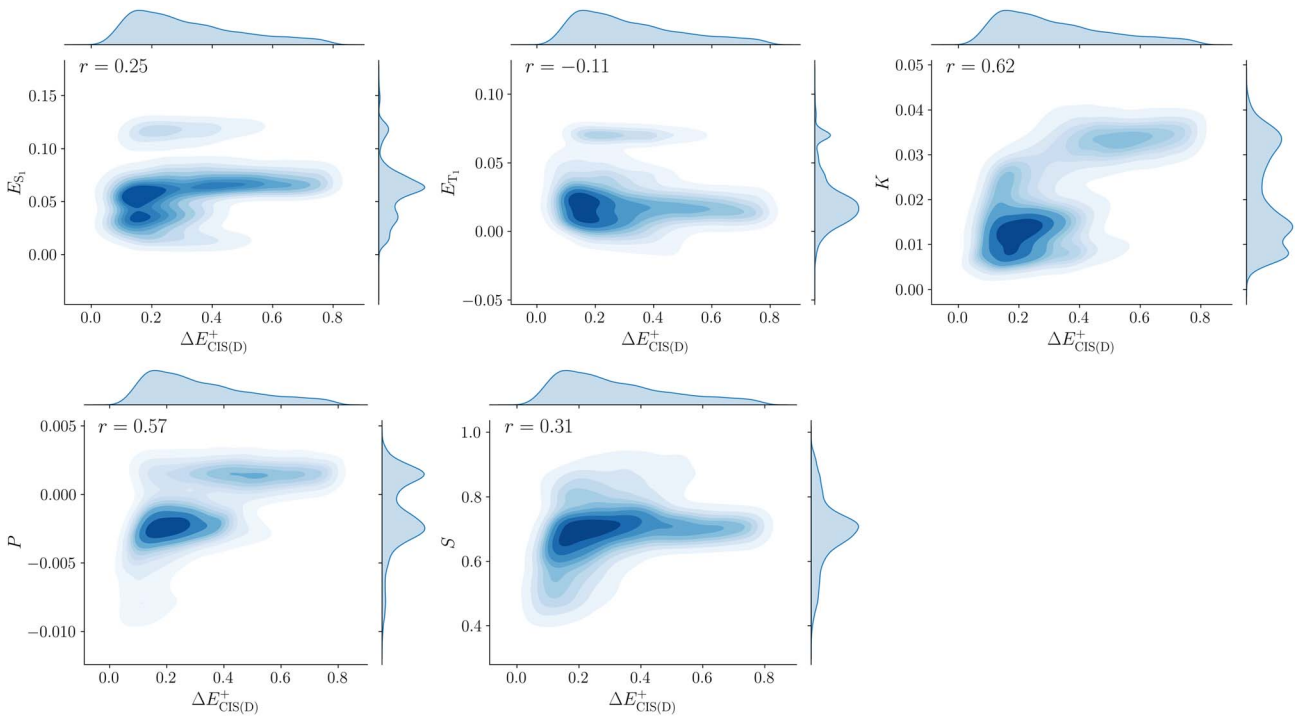

Fig. 4 Joint distribution plots illustrating the correlations between individual descriptors and positive ΔE_{ST}^{+} values, with kernel density estimation contours and correlation coefficients (r) displayed in each subplot to quantify the strength of the linear relationships.

To complement the SHAP results, we analyzed the joint distribution plots of each descriptor with the reference ΔE_{ST}^{+} values, as shown in Fig. 4. These plots corroborate the SHAP findings, revealing strong correlations for several features. The exchange integral K exhibits the strongest correlation ($r = 0.62$), followed closely by P ($r = 0.57$). Notably, the high correlation of P is unexpected given its lowest SHAP ranking, suggesting that it may play a synergistic role in concert with other descriptors. The overlap integral S shows a moderate positive correlation ($r = 0.31$), while E_{S_1} displays a weaker correlation ($r = 0.25$). E_{T_1} again shows a slight negative correlation ($r = -0.11$), consistent with both SHAP and physical interpretation. Interestingly, bimodal distributions in several of these descriptors indicate the presence of two distinct electronic state populations within the dataset, shedding light on the structural and electronic diversity of TADF emitters.

We further explored these descriptor interdependencies using Partial Least Squares (PLS) and Supervised PCA (SPCA) analyses to identify low-dimensional representations that retain most of the model's predictive power. As summarized in Table S2, the first PLS component alone accounts for 95.5% of the variance in the target variable while explaining 45.6% of the variance in the features. This component is heavily weighted by K (0.66), P (0.60), and S (0.33), with moderate influence from E_{S_1} (0.26) and a small negative loading from E_{T_1} (−0.12). This highlights the central role of exchange and spin polarization effects in governing ΔE_{ST}^{+}. Similarly, the SPCA analysis identifies K (0.72) and P (0.65) as the dominant contributors to the first component, which captures 74.8% of the total variance. The second component, explaining 13.4%, is shaped by S (0.60) and E_{S_1} (0.55), suggesting a secondary structure in the data related to orbital overlap and singlet energy levels. Collectively, these two components explain nearly 90% of the total variance, demonstrating that the essential physical factors influencing ΔE_{ST}^{+} can be represented in a reduced two-dimensional space driven primarily by K and P.

Taken together, these results provide strong, converging evidence for the key role of the exchange integral in tuning singlet–triplet gaps, with significant but more subtle contributions from spin polarization, orbital overlap, and excited-state energies. From a molecular design perspective, enhancing K provides a direct and effective strategy for widening the ΔE_{ST}^{+} gap, a critical factor for achieving efficient TADF emission. The prominence of P in both correlation and multivariate analyses further suggests that spin dynamics merit careful consideration.

3.2 Emitters with negative S_1–T_1 gap (ΔE_{ST}^{-})

For emitters with negative singlet–triplet energy gaps, we applied the same modeling protocol used for positive gaps (ΔE_{ST}^{+}). The SISSO modeling results, including the derived equations, coefficients, and performance metrics, are summarized in Table 1. Notably, the SISSO model for ΔE_{ST}^{-} achieved RMSE and maxAE values of 0.076 and 0.393, respectively, lower than those obtained for ΔE_{ST}^{+}. However, the Pearson correlation coefficient (r) for ΔE_{ST}^{-} was 0.665, reflecting room for further improvement despite the reduction in RMSE and maxAE. We integrated the SISSO-derived equation into a PIML model, resulting in significant improvements in predictive accuracy, as evidenced by the metrics reported in Table 2. The correlation coefficient r increased from 0.665 to 0.77 (testing set), while MAE and RMSE yielded 0.05 and 0.06, respectively. Fig. 5a and b illustrate the SISSO predictions and PIML test results, respectively, with Fig. S4 presenting the corresponding training predictions. We also evaluated the model's robustness using LOOCV, yielding r = 0.77, MAE = 0.05, and RMSE = 0.06, consistent with the PIML test set results (Table 2 and Fig. 5c).

We employed the same suite of model interpretable techniques used for positive gaps to interpret the PIML trained on emitters with negative singlet–triplet energy gaps. The goal was to uncover how the quantum descriptors' relative importance and mechanistic roles shift in this inverted regime. The SHAP summary plot (Fig. 5d) reveals a striking reordering of feature importance. Unlike the positive gap regime, where the exchange integral dominates, the singlet and triplet state energies emerge as the primary contributors. Both descriptors exhibit symmetric trends: higher values (in red) are consistently associated with more negative SHAP values, reinforcing their cooperative role in widening the negative gap. Interestingly, K plays a reversed role. While it amplified positive gaps previously, in this regime, lower K values (in blue) now contribute to larger negative gaps, as reflected by their negative SHAP values. In contrast, higher K values tend to suppress the extent of negativity. The overlap integral and dynamic spin polarization remain comparatively minor contributors, with narrow SHAP distributions centered around zero, signaling limited impact in the negative gap context.

These trends are quantitatively reinforced through joint distribution analysis. The strongest correlations are observed for E_{T_1} ($r = -0.54$) and E_{S_1} ($r = -0.52$), highlighting their nearly equal and inverse relationships with ΔE_{ST}^{-} (Fig. 6). This marks a fundamental departure from the positive gap model, where exchange interactions held primacy. K shows a mild positive correlation ($r = 0.18$), mirroring its dampening effect on negative gaps, while S ($r = -0.10$) and P ($r = -0.04$) display minimal direct associations with the target variable. As in the earlier case, bimodal distributions across several descriptors suggest the existence of two electronically distinct classes of molecules responsible for achieving negative gaps.

Multivariate decomposition *via* PLS and SPCA further underscores the mechanistic shift. As evident from Table S3, the first PLS component captures a remarkable 99.2% of target variance, with strong positive loadings for E_{T_1} (0.70) and E_{S_1} (0.67), and a modest negative contribution from K (−0.23). This singular component effectively encapsulates the governing physics. The SPCA results are in close agreement: the first component explains 91.8% of the variance, again dominated by E_{S_1} (0.69) and E_{T_1} (0.72). The consistency of these findings across methods confirms that excited state energies are the central drivers of negative ΔE_{ST} predictions.

These results indicate a fundamental transition in the electronic structure regime. While positive singlet–triplet gaps are shaped primarily by exchange interactions, negative gaps are governed by the absolute positions of the singlet and triplet

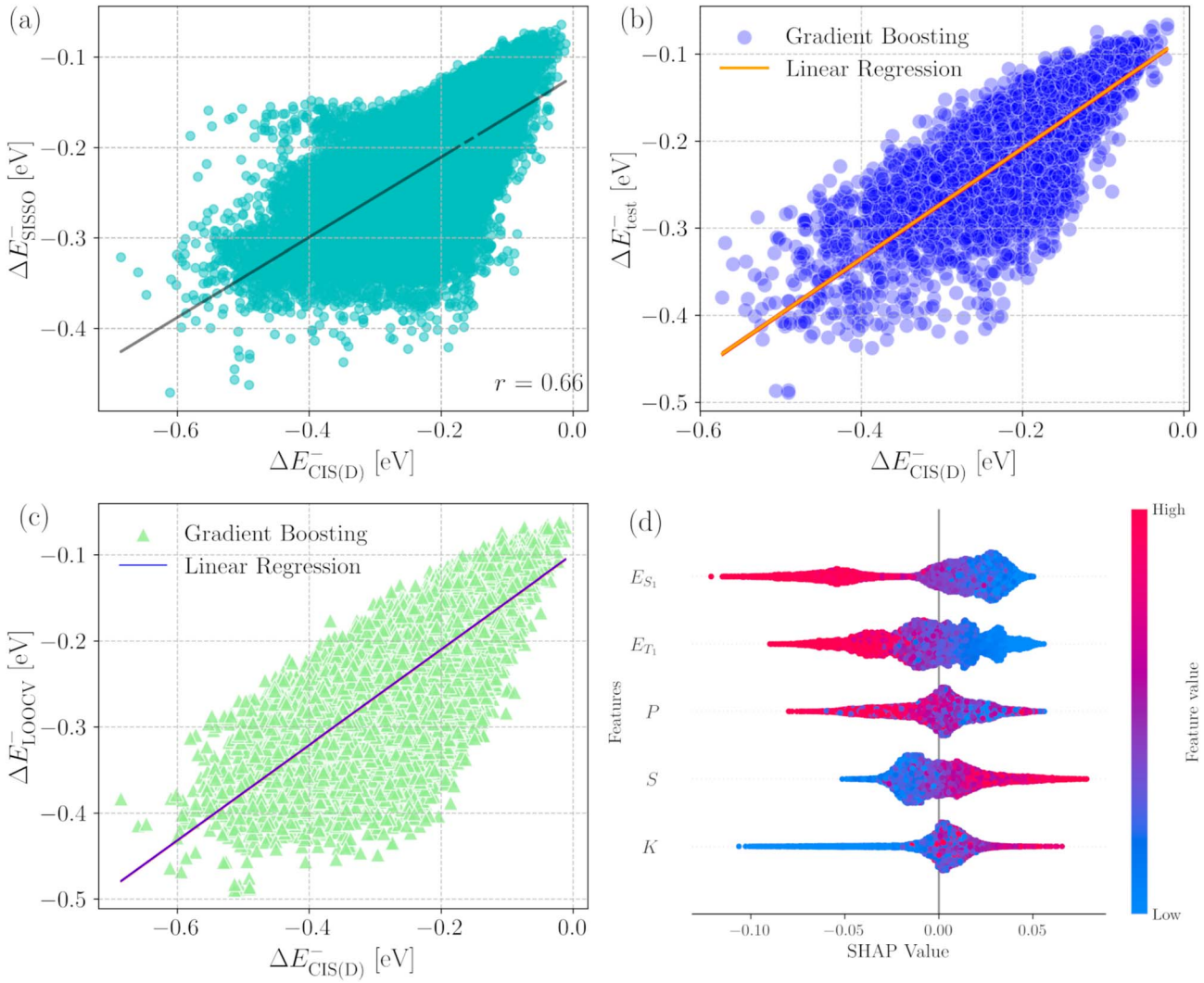

Fig. 5 Model evaluation and interpretability analysis for ΔE_{ST}^- prediction: (a) SISSO model performance, (b) PIML model performance on the testing dataset, (c) leave-one-out cross-validation results for model robustness assessment, and (d) SHAP analysis illustrating the feature contributions to ΔE_{ST}^- predictions.

excited states. From a design standpoint, this implies that to engineer molecules with negative singlet–triplet gaps—relevant for applications requiring inverted energy levels—one must focus on simultaneously elevating both E_{S_1} and E_{T_1} while minimizing exchange coupling. The near-equivalence of E_{S_1} and E_{T_1} in all analyses suggests that they should be considered a coupled pair, not in isolation.

3.3 Combined model for ΔE_{ST}

After separately analyzing the impact of different descriptors on ΔE_{ST} for both positive and negative cases, we extended our approach to a unified model incorporating all data points. Specifically, we sought to determine whether the model accuracy improves and if the consistency in descriptor importance is maintained when predicting ΔE_{ST} for the entire dataset. The key metrics from the SISSO modeling for this combined approach are summarized in Table 1. The combined model achieves a Pearson correlation coefficient of 0.747, surpassing the negative ΔE_{ST} model but falling short of the positive ΔE_{ST} model. Additionally, the maxAE and RMSE values are 1.088 and 0.207, respectively, higher than those in the individual models. Fig. 7a depicts the performance of the SISSO model for the combined dataset, while Fig. 7b shows the testing performance of the PIML model. The corresponding training performance is compared in Fig. S5. The combined model's test and training scores are presented in Table 2, where it achieves a Pearson correlation coefficient of 0.88, which is the highest among the three cases (positive, negative, and combined). However, its MAE and RMSE values are 0.11 and 0.14, respectively. Fig. 7c illustrates the LOOCV results, confirming a strong correlation between the predicted and target values.

To generalize our insights across the full range of singlet–triplet energy gaps, we applied the same SHAP and multivariate analyses to the combined dataset of positive and negative values. This unified approach captures the complex descriptor interactions that govern both conventional and INVEST-type TADF

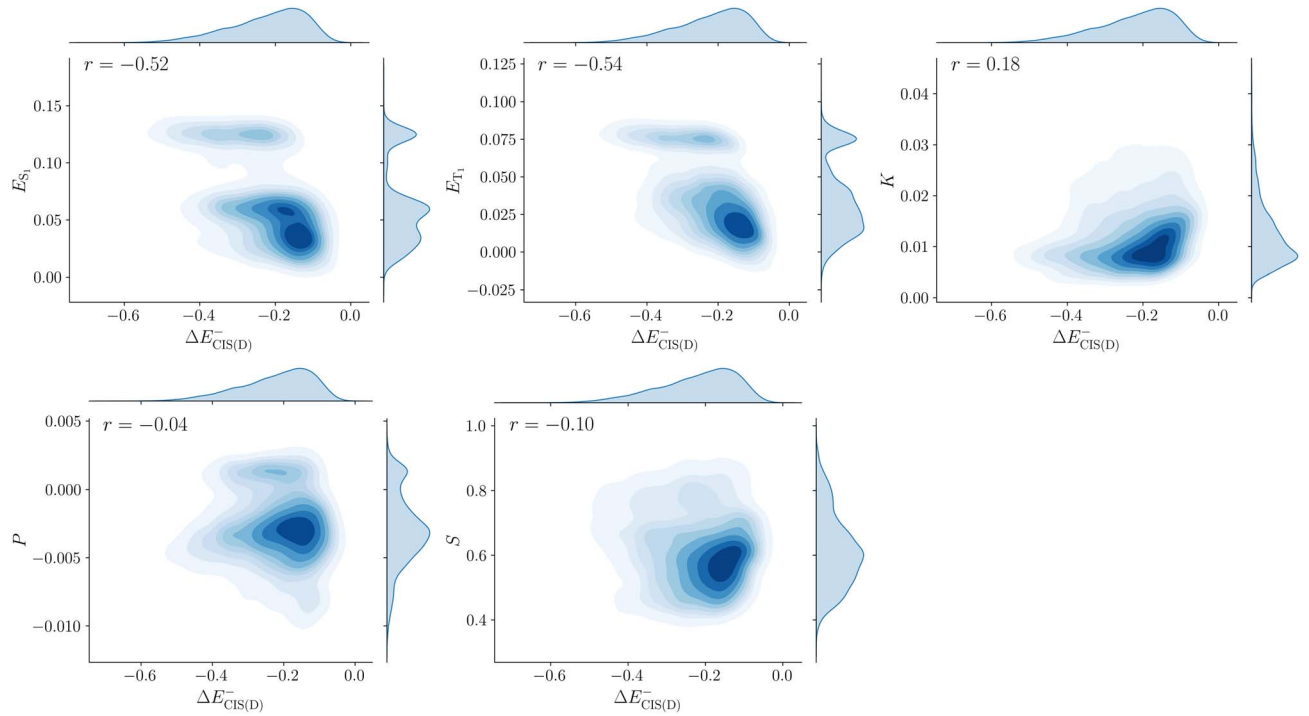

Fig. 6 Joint distribution plots illustrating the correlations between individual descriptors and ΔE_{ST}^{-} values, with kernel density estimation contours and correlation coefficients (r) displayed in each subplot to quantify the strength of the linear relationships.

emitters. Fig. 7d presents the SHAP summary plot, where the exchange integral continues to dominate the descriptor hierarchy. Its contribution exhibits pronounced asymmetry: large K values (in red) strongly favor positive SHAP values, reinforcing their influence in widening ΔE_{ST}, especially in conventional emitters. However, its effect diminishes in negative-gap systems, as indicated by a narrower and less impactful SHAP distribution. This attenuation reflects the altered electronic landscape of INVEST molecules, where inverted gaps arise from a different interplay of singlet energy and orbital reorganization, reducing the marginal role of exchange interactions.

The singlet excitation energy reveals a bipolar SHAP distribution, with high values tending toward negative SHAP contributions and low values contributing positively. This reflects its dual role: promoting inverted gaps in INVEST-like systems while supporting positive gaps in conventional architectures. The overlap integral also demonstrates a dispersed contribution pattern but with a net bias toward positive SHAP values, consistent with its role in modulating orbital coupling. The triplet excitation energy exhibits a wide SHAP spread, where higher values predominantly yield negative SHAP contributions, underscoring their association with reduced ΔE_{ST} in specific configurations. Polarization, while ranking lowest in the overall SHAP importance, still shows a context-dependent contribution. Its SHAP values are symmetrically distributed and centered near zero, with a mild skew toward negative contributions. This indicates a diminished but not negligible role in the combined model, likely due to the descriptor's variable relevance across chemically diverse TADF scaffolds.

These SHAP-derived trends are quantitatively supported by joint distribution plots, shown in Fig. 8. Among the descriptors, K exhibits the strongest positive correlation with ΔE_{ST} ($r = 0.60$), forming distinct bimodal clusters that separate conventional (positive ΔE_{ST}) and INVEST (negative ΔE_{ST}) regimes. This bimodality aligns with K's dominant SHAP ranking, where its asymmetric contributions highlight its crucial role in conventional systems while diminishing INVEST architectures. The excited-state energies display contrasting correlation patterns. E_{T_1} has a moderate negative correlation with ΔE_{ST} ($r = -0.33$). Similarly, E_{S_1} exhibits a weak overall correlation ($r = -0.04$), yet its SHAP distribution reveals a bipolar pattern, with both positive and negative contributions balancing each other. This explains why its linear correlation appears negligible despite its mechanistic significance. The overlap parameter shows a moderate positive correlation with ΔE_{ST} ($r = 0.37$), with higher S values aligning with positive ΔE_{ST} systems. Interestingly, P positively correlates ($r = 0.43$), which initially seems at odds with its bimodal SHAP profile. However, closer inspection reveals a symmetric SHAP distribution centered near zero, where high (red) and low (blue) values contribute across the spectrum. This explains P's reduced aggregate importance in the combined model despite its presence in $\Delta E_{ST} = 2K + P$: its influence is highly context-dependent, varying across molecular architectures.

Multivariate projections reinforce these findings, as summarized in Table S4. The first PLS component captures 80.3% of the variance, with substantial positive contributions from K, P, and S, and negative weights from E_{T_1} and E_{S_1}. This axis effectively separates molecules based on their dominant

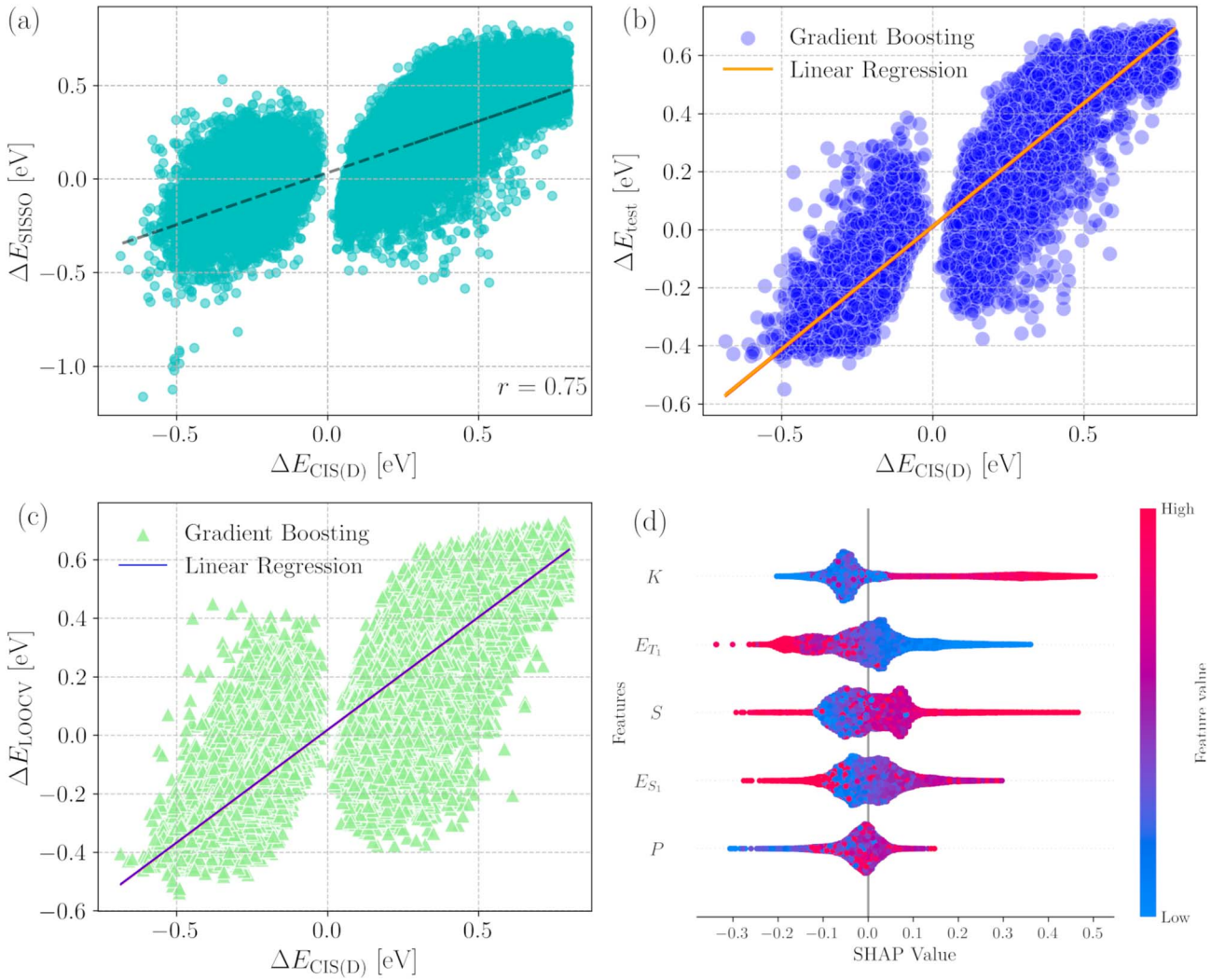

Fig. 7 Model evaluation and interpretability analysis for ΔE_{ST} prediction: (a) SISSO model performance, (b) PIML model performance on the testing dataset, (c) Leave-One-Out Cross-Validation (LOOCV) results for model robustness assessment, and (d) SHAP analysis illustrating the feature contributions to ΔE_{ST} predictions.

gap-driving mechanisms. The second and third components (3.1% and 5.4% variance, respectively) capture subtler interactions, particularly between polarization and excited state energies. SPCA reveals similar patterns: the first component (67.6%) is dominated by K and P, while the second (18.4%) emphasizes E_{T_1} and S. Together, they account for over 85% of the total variance, indicating that most of the underlying physics can be captured within a two-dimensional descriptor space shaped by exchange and excited-state characteristics.

Overall, these results establish that while K remains the primary driver of ΔE_{ST}, its dominance is modulated by the specific electronic configuration, particularly in molecules with inverted gaps. The consistent presence of bimodal distributions and shifting descriptor roles highlights the need for flexible models to accommodate both regimes. From a design standpoint, tuning the exchange integral remains the most direct route to gap modulation. However, achieving precise control—especially in the negative-gap regime—requires a delicate balancing of excited-state energies and orbital interactions. This holistic view provides a foundation for rational design strategies that span the entire landscape of TADF emitter architectures.

3.4 Oscillator strength (*f*)

After modeling and predicting ΔE_{ST}, our focus shifted toward investigating the oscillator strength, for which we developed a combined model using all available data points. Table 1 summarizes the SISSO modeling results for *f*, highlighting a fairly strong correlation with selected descriptors ($r = 0.714$). The model's accuracy is evident from its maxAE (0.341) and RMSE (0.034), with the correlation plot shown in Fig. 9a. The performance metrics for PIML are provided in Table 2. The correlation coefficient significantly increased to 0.84, while the RMSE and MAE values yielded 0.03 and 0.02 for the test dataset. Fig. 9b illustrates the test set correlation plot, while the training set correlation is shown in Fig. S6. To validate the model's robustness, we performed LOOCV, as illustrated in Fig. 9c, demonstrating strong agreement between predicted and actual values.

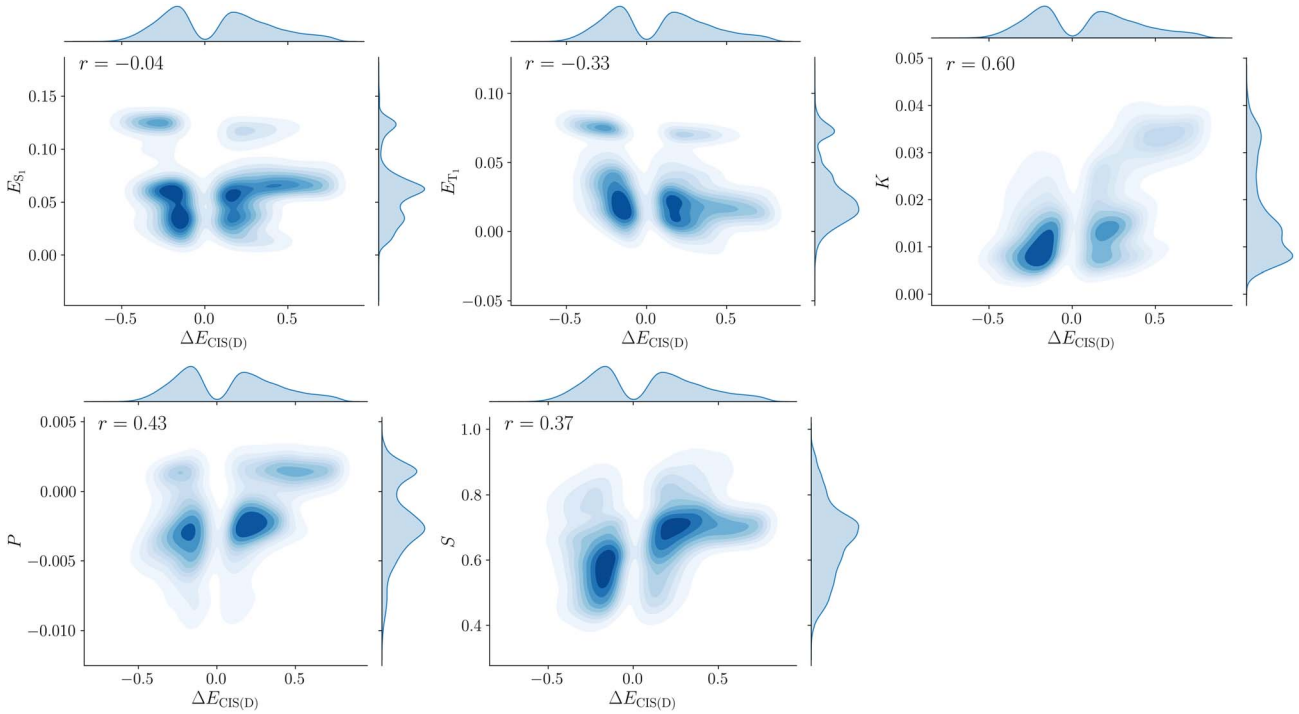

Fig. 8 Joint distribution plots illustrating the correlations between individual descriptors and combined ΔE_{ST} values, with kernel density estimation contours and correlation coefficients (r) displayed in each subplot to quantify the strength of the linear relationships.

The SHAP summary plot (Fig. 9d) establishes a clear descriptor hierarchy for oscillator strength predictions. The exchange integral dominates, displaying a consistently strong positive influence—higher K values (red) are associated with significant positive SHAP values. This directional trend affirms K's role in enhancing oscillator strength *via* modulation of transition dipole moments, which aligns with electronic structure principles. The sharp asymmetry in SHAP values further underscores K's centrality to optical transition intensity. E_{S_1} exhibits a bipolar SHAP distribution, reflecting context-dependent contributions that vary with molecular configurations. E_{T_1}, by contrast, consistently contributes negatively—higher E_{T_1} values reduce oscillator strength, likely due to diminished singlet–triplet mixing. S and P show smaller but non-negligible effects, both centered near zero, with P displaying a slight skew toward positive contributions.

As evident from Fig. 10, joint distribution plots support these insights: K exhibits the strongest correlation with oscillator strength ($r = 0.54$), followed by P ($r = 0.35$) and S ($r = 0.33$). E_{T_1} displays a modest inverse correlation ($r = -0.24$), while E_{S_1} remains largely uncorrelated ($r = 0.03$). These trends point to distinct electronic subpopulations governing oscillator strength, reinforcing the diversity of contributing mechanisms. Multivariate analyses further clarify these roles. In the PLS decomposition (Table S5), the first component explains 88% of target variance, driven predominantly by K (0.74) and P (0.60), with a negative weight from E_{T_1} (−0.23). The second component (5.4%) is dictated by S (0.94), suggesting a secondary contribution *via* orbital overlap, while the third (2.27%) reflects a combined influence of E_{S_1} (0.84) and E_{T_1} (0.53), highlighting energy-level dependent fine-tuning. SPCA corroborates these findings. Its first component (78.5% variance) confirms K (0.79) and P (0.59) as primary descriptors. The second (13.8%) reveals a competitive interplay between P (0.77) and K (−0.56), suggesting configuration-specific antagonism. The third (6%) again elevates E_{T_1} (0.79) and S (0.44), emphasizing tertiary mechanisms involving excited state positioning and electronic overlap.

Altogether, these analyses converge on a robust mechanistic model: the exchange integral is the key driver of oscillator strength, supported by dynamic spin polarization and modulated by E_{T_1} and S in specific configurations. This reflects an intricate interdependence between exchange effects, excited state energies, and spatial orbital interactions. From a design standpoint, enhancing oscillator strength in TADF emitters requires maximizing K and P while carefully managing E_{T_1}. Importantly, these parameters should not be tuned in isolation—interdependencies highlighted by multivariate decomposition indicate the need for coordinated optimization strategies. By bridging machine learning interpretability with quantum chemical theory, this analysis not only delivers accurate oscillator strength predictions but also deepens our mechanistic understanding, guiding the rational design of TADF materials with superior light-matter coupling for advanced optoelectronic applications.

3.5 Cross validation: external datasets

To thoroughly evaluate the diversity, predictive accuracy, and robustness of our combined model for ΔE_{ST} and f, we extended the validation process beyond LOOCV by testing the model on external datasets. Specifically, we utilized a dataset of

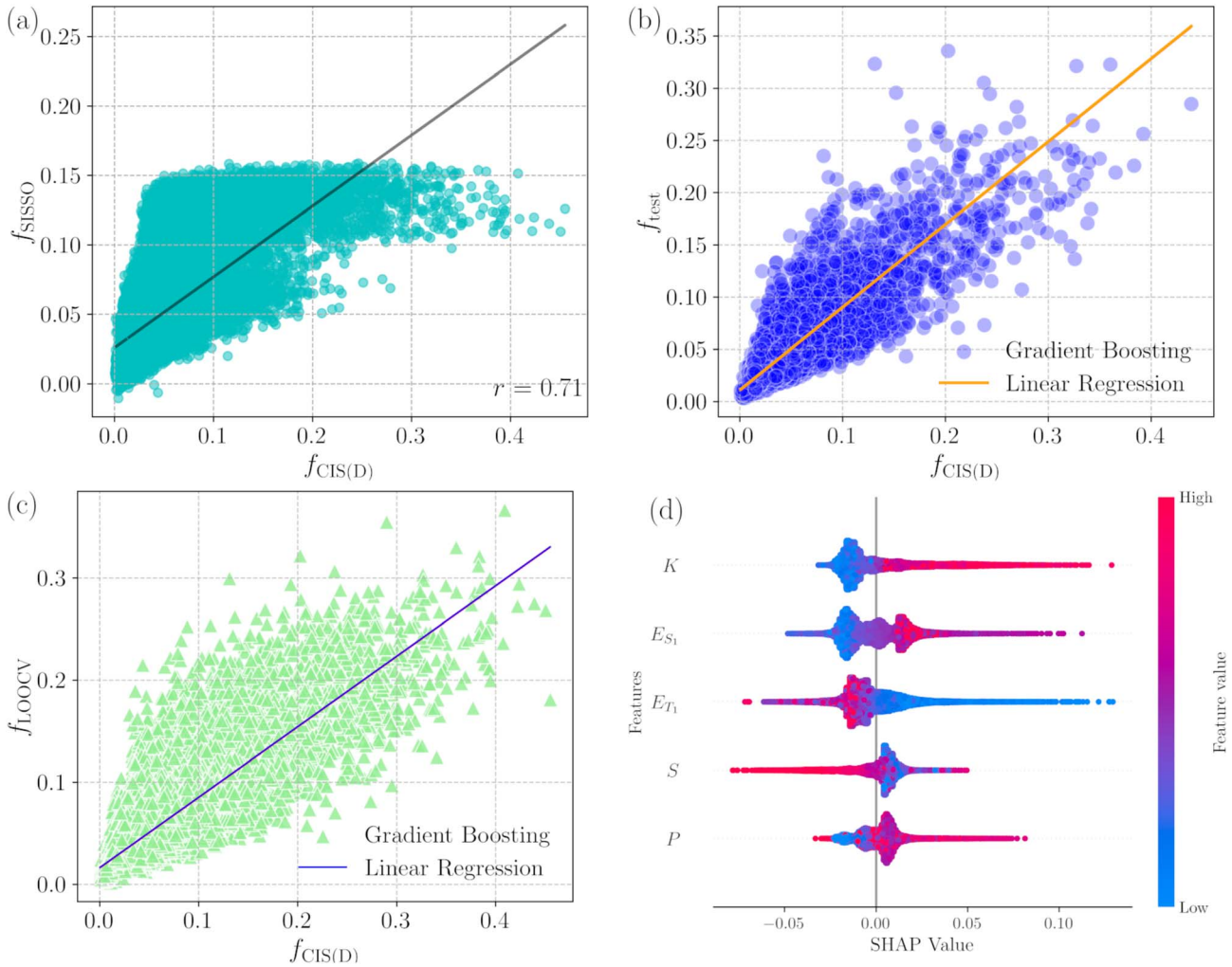

Fig. 9 Model evaluation and interpretability analysis for f prediction: (a) SISSO model performance, (b) PIML model performance on the testing dataset, (c) Leave-One-Out Cross-Validation (LOOCV) results for model robustness assessment, and (d) SHAP analysis illustrating the feature contributions to f predictions.

approximately 110 compounds, drawn from recent studies,[22,23] where ΔE_{ST} values were computed at the CC2/aug-cc-pVDZ level of theory—a level distinct from the one used for training the model. We calculated the required five descriptors for each molecule in this dataset using PPP-based calculations and then applied the combined model to predict ΔE_{ST} (Dataset-III). The results, illustrated in Fig. 11, reveal a robust correlation between the predicted and reference ΔE_{ST} values, with a correlation coefficient of 0.80. The RMSE and MAE values also remained below 0.1 eV, underscoring the model's strong predictive capabilities across chemically diverse systems. To further assess the model's accuracy, we conducted an independent evaluation on a smaller dataset of 28 compounds, for which experimental ΔE_{ST} values were available from previous studies (Dataset-IV).[4,48–60] The detailed results, summarized in Table S6, are equally promising: the MAE and RMSE for this evaluation were 0.046 eV and 0.054 eV, respectively. These values are comparable to—and, in most cases, outperform—results obtained using more computationally demanding methods such as SCS-CC2, STEOM-DLPNO-CCSD, and B2LYP.[33,43] Notably, the maximum absolute error remained below 0.1 eV, reaffirming the robustness of our model.

Given the significance of oscillator strength in emission studies, we also sought to validate the model's predictive performance for this property. However, because neither experimental f values nor high-level computational results were available in the literature for external datasets, we primarily relied on LOOCV for validation. As part of this analysis, we predicted oscillator strength values for the same set of 110 molecules, providing insights into f's variation across diverse chemical structures (Fig. S7). Although this exercise did not serve as an independent benchmark, it reinforces confidence in the model's broader applicability and predictive reliability. Overall, the successful prediction of ΔE_{ST} for external datasets—along with the consistency observed in LOOCV and test set results for both ΔE_{ST} and f—demonstrates the model's robustness, adaptability, and potential utility in future studies of diverse molecular systems.

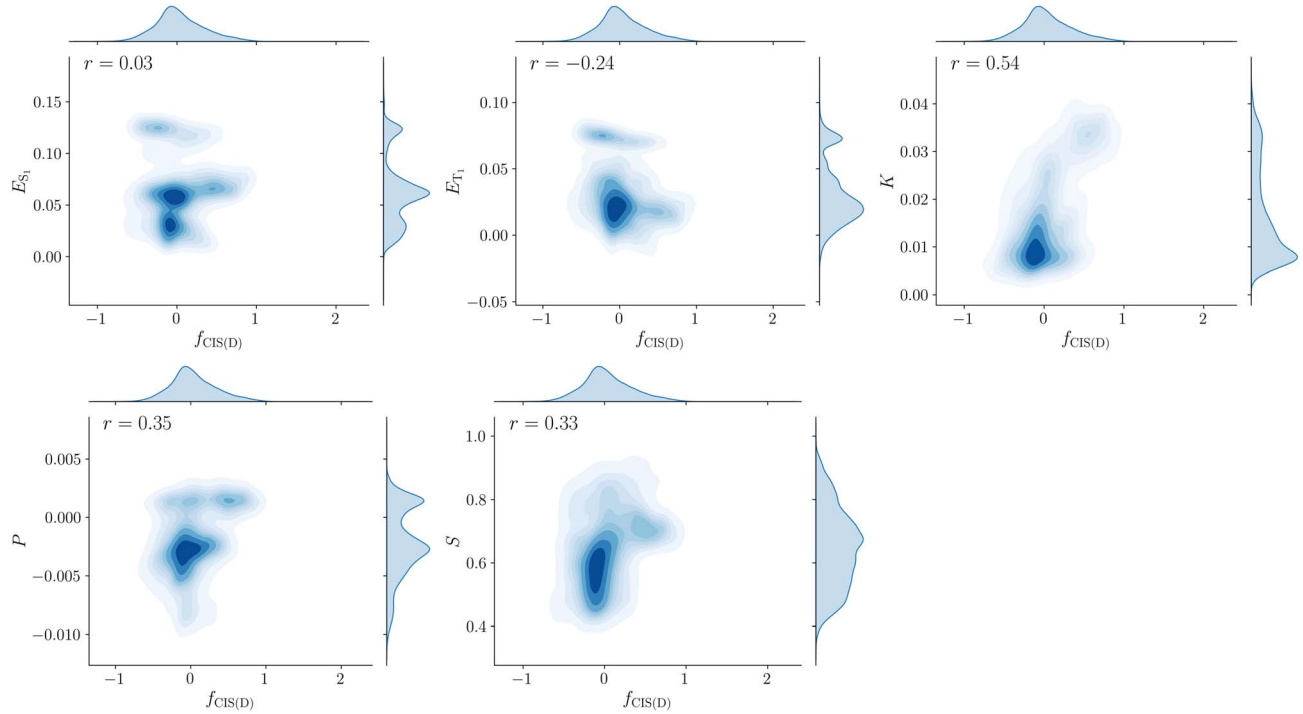

Fig. 10 Joint distribution plots illustrating the correlations between individual descriptors and negative *f* values, with kernel density estimation contours and correlation coefficients (*r*) displayed in each subplot to quantify the strength of the linear relationships.

3.6 High-throughput screening enabled by physics-informed ML models

To further establish the practical utility of our physics-informed machine learning models, we extended their application to the high-throughput screening of unexplored emitters for organic light-emitting diode applications. Building upon the predictive reliability demonstrated in our prior work,[34] we employed our custom gradient boosting models—optimized for both singlet–triplet energy gap and oscillator strength—to assess a newly curated set of candidate molecules, herein referred to as Dataset-V. This dataset comprises 400 computationally designed TADF emitters generated through the systematic recombination of high-performing molecular fragments (Fig. S8) reported in the literature.[21–23] These fragments, which have been experimentally validated or computationally demonstrated to contribute favorably to TADF or INVEST behavior, were carefully selected to ensure chemical relevance and structural diversity. Unique atomic tags were employed during the assembly process to enable precise identification and reliable reconstruction of the molecules. Symmetric and asymmetric terminal fragment combinations were incorporated, enriching the chemical space explored through this dataset. For each of these 400 emitters, all five essential descriptors were computed following the same protocol outlined in Section 2.1.

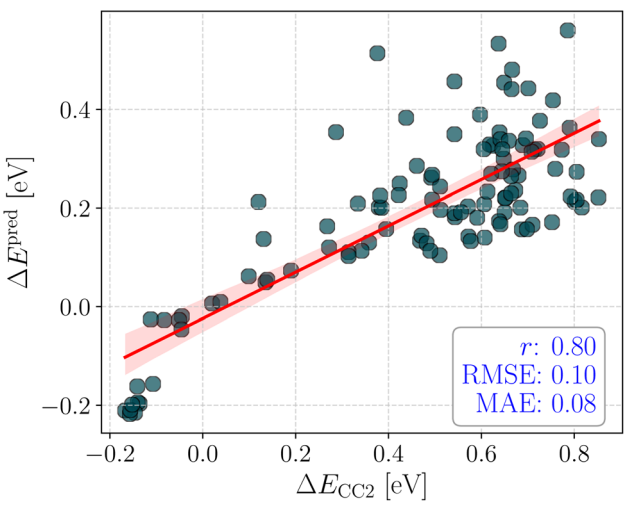

Fig. 11 External validation of the combined model for ΔE_{ST} predictions. The scatter plot compares predicted ΔE_{ST} values against reference data from an independent dataset of 110 compounds computed at the CC2/aug-cc-pVDZ level of theory.[22,23] The strong correlation ($r = 0.80$), along with RMSE and MAE values below 0.1 eV, demonstrates the model's predictive accuracy and robustness across chemically diverse systems.

The outcomes of this screening exercise were both encouraging and informative. Our model predicted that 93.8% of the designed compounds exhibit conventional TADF characteristics, whereas 6.2% fall into the category of inverted singlet–triplet gap emitters, representing a particularly intriguing subclass for optoelectronic applications. The predicted ΔE_{ST} values ranged from −0.13 eV to 0.28 eV, with a median value of 0.13 eV and an average of 0.12 eV. A standard deviation of 0.07 eV reflects the internal consistency and reliability of the model across this diverse chemical space. Similarly, the

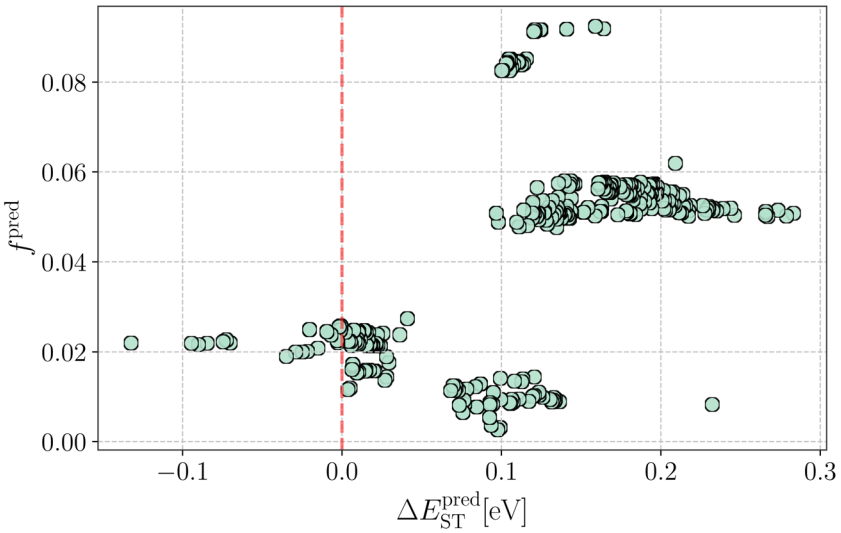

Fig. 12 Two-dimensional distribution of predicted singlet–triplet energy gap (ΔE_{ST}) and oscillator strength (f) for 400 computationally designed emitters (Dataset-V). The predictions were generated using the optimized physics-informed gradient boosting models. The red vertical dotted line separates the INVEST candidates from their conventional TADF counterparts.

predicted f values spanned from 0.003 to 0.092, highlighting the broad optoelectronic potential of these designs.

A two-dimensional distribution of the predicted ΔE_{ST} (x-axis) and f (y-axis) for all 400 emitters is shown in Fig. 12. This plot delineates a subset of promising candidates that strike a favorable balance between small singlet–triplet gaps and high oscillator strengths. Among these, 44 emitters were identified as especially promising, featuring ΔE_{ST} values below 0.2 eV and f values exceeding 0.08—a combination indicative of superior photophysical performance and suitability for high-efficiency OLED applications. The molecular structures of the 12 promising candidates from this group are presented in Fig. S9, offering concrete examples of how fragment-based design, coupled with accurate PIML predictions, can accelerate material discovery.

To validate the reliability of our PIML model, we selected four representative candidates and computed their ΔE_{ST} and f values using the CIS(D) method in ORCA 5.0.3.[61] As shown in Table S7, the predicted singlet–triplet gaps show good agreement with CIS(D) results, typically within 0.1 eV. While the model slightly overestimates oscillator strengths, the overall ranking and identification of promising emitters remain consistent, supporting the model's robustness for high-throughput screening.

In summary, this screening exercise underscores the strength and robustness of our physics-informed machine learning framework, which delivers accurate predictions and enables efficient navigation of chemical space. By leveraging physically meaningful descriptors derived from reliable quantum-chemical approximations, this approach facilitates the rapid identification of new emitter candidates, significantly reducing the computational cost and time typically associated with excited-state property evaluation. Our results demonstrate the potential of this strategy to drive accelerated discovery and rational design of next-generation materials for organic electronics.

3.7 Extended analyses: model robustness, descriptor interpretability, and physical insight

We conducted a series of complementary analyses to evaluate further the robustness, interpretability, and generalizability of our physics-informed machine learning framework. These efforts address potential concerns related to dataset composition, descriptor interdependencies, physical interpretability, and benchmarking against existing models.

To assess the impact of class imbalance in our dataset (55.8% TADF *vs.* 44.2% INVEST), we evaluated three mitigation strategies: stratified sampling, class weighting, and undersampling with reweighting. Our baseline model, trained without explicit imbalance correction, already achieved strong performance (overall $r = 0.881$) with balanced accuracy across classes, consistent with best practices for mild imbalance (ratio $\sim$1.26 : 1). The alternative strategies yielded only marginal improvements ($\leq$0.09% in r) while slightly narrowing the TADF–INVEST performance gap. Consequently, we retained the baseline architecture as the default, as it preserves class proportions without introducing synthetic bias. Full methodological details and comparative results are provided in Section S2, Fig. S10, and Table S8.

To rule out the effects of multicollinearity among the five PPP-derived descriptors (E_{S_1}, E_{T_1}, K, S, and P), we performed correlation and variance inflation factor (VIF) analyses. While a strong correlation was observed between E_{S_1} and E_{T_1} ($r = 0.905$), all other pairs remained below $|r| = 0.7$, and corresponding VIFs were within acceptable limits. A Gram–Schmidt orthogonalization further confirmed that this collinearity could be removed without affecting the descriptor matrix structure. However, Optuna-guided hyperparameter tuning consistently produced models with equivalent performance (ΔRMSE < 0.001 eV) on both native and orthogonalized inputs, demonstrating that the Gradient Boosting model effectively regularizes the

modest correlation. As the remaining dependencies are physically interpretable and the native form retains quantum-chemical transparency, we retain the original descriptors in the final model. Complete analyses are presented in Section S3, Fig. S11 and S12.

To elucidate how molecular features influence the exchange integral (K), we examined structure–property relationships through systematic variations in donor–acceptor geometry, heteroatom substitution, and core aromaticity. Torsional scans between donor and acceptor fragments revealed that both K and the dynamic spin polarization (P) reach maxima at planar geometries, highlighting the role of conjugation and orbital overlap (Fig. S13). Density difference plots for ten representative emitters demonstrated that subtle differences in orbital topology can yield significantly different K values, even for molecules with similar charge transfer characteristics—emphasizing the limitations of visual analysis alone (Fig. S14). Furthermore, we found that sulfur-bridged compounds exhibit larger dihedral angles than their oxygen-bridged counterparts, which weakens planarity and reduces HOMO–LUMO overlap, thereby lowering K (Fig. S15). Core aromaticity also modulates conjugation: less aromatic units like pyrrole enhance K and P relative to more aromatic benzene cores. Together, these results provide a nuanced physical understanding of how geometry and electronic structure modulate excited-state interactions, offering rational strategies for tuning K in TADF emitters.

To benchmark our model against established physics-enhanced methods, we implemented a Δ-ML approach using SchNet[62] neural networks trained on the same dataset and descriptors. Compared to SchNet, our PIML model exhibited significantly higher accuracy ($r = 0.88$ *vs.* 0.61; MAE = 0.11 eV *vs.* 0.20 eV) along with enhanced interpretability, efficiency, and adherence to physical constraints—hallmarks of a robust and integrated learning framework. A complete analysis is provided in Section S4, Fig. S16, S17 and Table S9.

Finally, our model—built upon PPP-derived descriptors—offers a computationally efficient yet accurate approach for predicting singlet–triplet gaps and oscillator strengths at a CIS(D)-level of fidelity. Unlike prior studies that relied solely on quantum chemical screening,[26] our method establishes a physics-informed mapping from semi-empirical inputs to excited-state properties. The model aligns well with reference CIS(D) and experimental data, and its predictive utility was further demonstrated by accurate inference on newly designed molecules, underscoring its potential for prospective high-throughput screening of organic emitters.

4 Conclusion

This study highlights the effectiveness of physics-informed machine learning in accurately predicting key photophysical properties—specifically the singlet–triplet energy gap (ΔE_{ST}) and oscillator strength (f)—that critically determine the performance of both thermally activated delayed fluorescence and emerging inverted singlet–triplet emitters. Leveraging a chemically diverse dataset of approximately 39 000 molecular systems, we systematically developed dedicated models to address the prediction of positive, negative, and full-range ΔE_{ST} values, enabling a comprehensive exploration of emitter types. Interestingly, while property-specific models offer deeper mechanistic insight into molecular behavior, their predictive performance remains comparable to that of a unified, combined model, suggesting that integrated learning strategies can achieve both generality and computational efficiency without sacrificing interpretability.

Beyond predictive performance, interpretability tools consistently revealed exchange interaction, dynamic spin polarization, and excited-state energies as the key descriptors governing both ΔE_{ST} and oscillator strength. In particular, the central role of exchange interactions emerged as a recurring theme across all models, reinforcing its mechanistic relevance to both radiative and non-radiative pathways in emitter design. This physical consistency across methods reinforces the reliability of the learned relationships. Leveraging this framework, we further demonstrated the practical utility of our models through high-throughput screening of 400 newly designed emitters. The screening successfully identified a promising subset of candidates exhibiting favorable combinations of small ΔE_{ST} and high oscillator strength, highlighting the model's capability to accelerate the discovery of efficient TADF and INVEST materials.

Altogether, our findings underscore the importance of embedding physical knowledge into machine learning models to enhance predictive accuracy and interpretability. The resulting framework not only enables rapid molecular screening but also offers actionable design principles for the targeted development of high-performance emitters. This work manifests how data-driven and theory-guided approaches can be integrated to bridge the gap between predictive modeling and rational material innovation.

Author contributions

AM conceived and supervised the project. Sanyam and BD performed the simulations and analyzed the results. Sanyam, BD, and AM prepared the draft of the manuscript.

Conflicts of interest

There are no conflicts to declare.

Data availability

The data and code to reproduce the results are available in our GitHub repository (**https://github.com/Bib569/TADF-ML-Discovery**).

Supplementary information: The performance of the PIML model on the training set, predicted oscillator strengths for 110 molecules, and the molecular fragments used to design 400 candidate structures, along with 12 standout emitters selected from the top 44 high-performing compounds. It includes a comprehensive table of SISSO models from 1D to 3D for key target properties, PLS and Supervised PCA component analysis, and a comparative table of experimental and predicted ΔE_{ST}

values for a dataset of 28 molecules. Also, it contains PIML architecture and workflow, class imbalance analysis, multicollinearity assessment, Δ-ML framework, and density difference plot. See DOI: https://doi.org/10.1039/d5ta03374h.

Acknowledgements

The authors gratefully acknowledge the Indian Institute of Technology Gandhinagar, India, for providing research facilities and financial support. Sanyam thanks CSIR for the fellowship. We thank PARAM Ananta for computational resources.

References

1 A. Endo, K. Sato, K. Yoshimura, T. Kai, A. Kawada, H. Miyazaki and C. Adachi, Efficient up-conversion of triplet excitons into a singlet state and its application for organic light emitting diodes, *Appl. Phys. Lett.*, 2011, **98**, 083302.

2 Y. Liu, C. Li, Z. Ren, S. Yan and M. R. Bryce, All-organic thermally activated delayed fluorescence materials for organic light-emitting diodes, *Nat. Rev. Mater.*, 2018, **3**, 18020.

3 H. Uoyama, K. Goushi, K. Shizu, H. Nomura and C. Adachi, Highly efficient organic light-emitting diodes from delayed fluorescence, *Nature*, 2012, **492**, 234–238.

4 Y. Xu, Z. Cheng, Z. Li, B. Liang, J. Wang, J. Wei, Z. Zhang and Y. Wang, Molecular-structure and device-configuration optimizations toward highly efficient green electroluminescence with narrowband emission and high color purity, *Adv. Opt. Mater.*, 2020, **8**, 1902142.

5 Y. Xu, C. Li, Z. Li, Q. Wang, X. Cai, J. Wei and Y. Wang, Constructing Charge-Transfer Excited States Based on Frontier Molecular Orbital Engineering: Narrowband Green Electroluminescence with High Color Purity and Efficiency, *Angew. Chem.*, 2020, **59**, 17442–17446.

6 K. Goushi, K. Yoshida, K. Sato and C. Adachi, Organic light-emitting diodes employing efficient reverse intersystem crossing for triplet-to-singlet state conversion, *Nat. Photonics*, 2012, **6**, 253–258.

7 P. Stachelek, J. S. Ward, P. L. dos Santos, A. Danos, M. Colella, N. Haase, S. J. Raynes, A. S. Batsanov, M. R. Bryce and A. P. Monkman, Molecular Design Strategies for Color Tuning of Blue TADF Emitters, *ACS Appl. Mater. Interfaces*, 2019, **11**, 27125–27133.

8 S. Izumi, H. F. Higginbotham, A. Nyga, P. Stachelek, N. Tohnai, P. d. Silva, P. Data, Y. Takeda and S. Minakata, Thermally activated delayed fluorescent donor–acceptor–donor–acceptor π-conjugated macrocycle for organic light-emitting diodes, *J. Am. Chem. Soc.*, 2020, **142**, 1482–1491.

9 Y.-H. Kim, D.-C. Shin, S.-H. Kim, C.-H. Ko, H.-S. Yu, Y.-S. Chae and S.-K. Kwon, Novel blue emitting material with high color purity, *Adv. Mater.*, 2001, **13**, 1690–1693.

10 H. Jung, H. Lee, S. Kang, B.-K. An, K. S. Yook, Y.-I. Park, B. Kim and J. Park, Recent progress on organic emitters for organic light emitting diode lightings, *Appl. Chem. Eng.*, 2016, **27**, 455–466.

11 Z. Gao, Y. Liu, Z. Wang, F. Shen, H. Liu, G. Sun, L. Yao, Y. Lv, P. Lu and Y. Ma, High-efficiency violet-light-emitting materials based on phenanthro [9, 10-d] imidazole, *Chem.–Eur. J.*, 2013, **19**, 2602.

12 Z. Gao, G. Cheng, F. Shen, S. Zhang, Y. Zhang, P. Lu and Y. Ma, Highly efficient deep blue light emitting devices based on triphenylsilane modified phenanthro [9, 10-d] imidazole, *Laser Photonics Rev.*, 2014, **8**, L6–L10.

13 H. Jung, S. Kang, H. Lee, Y.-J. Yu, J. H. Jeong, J. Song, Y. Jeon and J. Park, High efficiency and long lifetime of a fluorescent blue-light emitter made of a pyrene core and optimized side groups, *ACS Appl. Mater. Interfaces*, 2018, **10**, 30022–30028.

14 H. Bi, K. Ye, Y. Zhao, Y. Yang, Y. Liu and Y. Wang, Fluorinated quinacridone derivative based organic light-emitting device with high power efficiency, *Org. Electron.*, 2010, **11**, 1180–1184.

15 H. U. Kim, H. J. Jang, W. Choi, M. Kim, S. Park, T. Park, J. Y. Lee and K. Bejoymohandas, Ancillary ligand-assisted robust deep-red emission in iridium (III) complexes for solution-processable phosphorescent OLEDs, *J. Mater. Chem. C*, 2019, **7**, 4143–4154.

16 A. Hohenleutner, S. Schmidbauer, R. Vasold, D. Joosten, P. Stoessel, H. Buchholz and B. König, Rapid combinatorial synthesis and chromatography based screening of phosphorescent iridium complexes for solution processing, *Adv. Funct. Mater.*, 2012, **22**, 3406–3413.

17 G. Li, T. Fleetham, E. Turner, X.-C. Hang and J. Li, Highly efficient and stable narrow-band phosphorescent emitters for OLED applications, *Adv. Opt. Mater.*, 2015, **3**, 390–397.

18 R. Ilmi, M. S. Khan, W. Sun, L. Zhou, W.-Y. Wong and P. R. Raithby, A single component white electroluminescent device fabricated from a metallo-organic terbium complex, *J. Mater. Chem. C*, 2019, **7**, 13966–13975.

19 Sanyam, R. Khatua and A. Mondal, Constructing Multiresonance Thermally Activated Delayed Fluorescence Emitters for Organic LEDs: A Computational Investigation, *J. Phys. Chem. A*, 2023, **127**, 10393–10405.

20 R. Nikhitha and A. Mondal, Breaking the trade-off between ΔE_{ST} and oscillator strength in hybrid LR/SR-CT compounds for enhanced TADF performance, *J. Mater. Chem. C*, 2025, **13**, 1893–1906.

21 Sanyam, P. Sorout and A. Mondal, Rational Design of Organic Emitters with Inverted Singlet–Triplet Gaps for Enhanced Exciton Management, *J. Phys. Chem. A*, 2024, **128**, 7114–7123.

22 M. H. Garner, J. T. Blaskovits and C. Corminboeuf, Double-bond delocalization in non-alternant hydrocarbons induces inverted singlet–triplet gaps, *Chem. Sci.*, 2023, **14**, 10458–10466.

23 M. H. Garner, J. T. Blaskovits and C. Corminboeuf, Enhanced inverted singlet–triplet gaps in azaphenalenes and non-alternant hydrocarbons, *ChemComm*, 2024, **60**, 2070–2073.

24 J. Terence Blaskovits, M. H. Garner and C. Corminboeuf, Symmetry-Induced Singlet-Triplet Inversions in Non-

Alternant Hydrocarbons, *Angew. Chem.*, 2023, **135**, e202218156.
25 K. Jorner, R. Pollice, C. Lavigne and A. Aspuru-Guzik, Ultrafast Computational Screening of Molecules with Inverted Singlet–Triplet Energy Gaps Using the Pariser–Parr–Pople Semiempirical Quantum Chemistry Method, *J. Phys. Chem. A*, 2024, **128**, 2445–2456.
26 R. Pollice, B. Ding and A. Aspuru-Guzik, Rational design of organic molecules with inverted gaps between the first excited singlet and triplet, *Matter*, 2024, **7**, 1161–1186.
27 A. Mahmood and J.-L. Wang, Machine learning for high performance organic solar cells: current scenario and future prospects, *Energy Environ. Sci.*, 2021, **14**, 90–105.
28 G. Zhang, F. R. Lin, F. Qi, T. Heumüller, A. Distler, H.-J. Egelhaaf, N. Li, P. C. Chow, C. J. Brabec, A. K.-Y. Jen and H.-L. Yip, Renewed prospects for organic photovoltaics, *Chem. Rev.*, 2022, **122**, 14180–14274.
29 X. Rodríguez-Martínez, E. Pascual-San-José and M. Campoy-Quiles, Accelerating organic solar cell material's discovery: high-throughput screening and big data, *Energy Environ. Sci.*, 2021, **14**, 3301–3322.
30 A. Pershin, D. Hall, V. Lemaur, J.-C. Sancho-Garcia, L. Muccioli, E. Zysman-Colman, D. Beljonne and Y. Olivier, Highly emissive excitons with reduced exchange energy in thermally activated delayed fluorescent molecules, *Nat. Commun.*, 2019, **10**, 597.
31 D. Hall, S. M. Suresh, P. L. dos Santos, E. Duda, S. Bagnich, A. Pershin, P. Rajamalli, D. B. Cordes, A. M. Slawin, D. Beljonne, K. Anna, I. D. W. Samuel, Y. Olivier and E. Zysman-Colman, Improving processability and efficiency of resonant TADF emitters: a design strategy, *Adv. Opt. Mater.*, 2020, **8**, 1901627.
32 S. M. Suresh, E. Duda, D. Hall, Z. Yao, S. Bagnich, A. M. Slawin, H. Bässler, D. Beljonne, M. Buck, Y. Olivier, A. Köhler and E. Zysman-Colman, A deep blue B, N-doped heptacene emitter that shows both thermally activated delayed fluorescence and delayed fluorescence by triplet–triplet annihilation, *J. Am. Chem. Soc.*, 2020, **142**, 6588–6599.
33 D. Hall, J. C. Sancho-García, A. Pershin, G. Ricci, D. Beljonne, E. Zysman-Colman and Y. Olivier, Modeling of multiresonant thermally activated delayed fluorescence emitters properly accounting for electron correlation is key, *J. Chem. Theory Comput.*, 2022, **18**, 4903–4918.
34 R. Khatua, B. Das and A. Mondal, Physics-Informed Machine Learning with Data-Driven Equations for Predicting Organic Solar Cell Performance, *ACS Appl. Mater. Interfaces*, 2024, **16**, 57467–57480.
35 H. Tang, B. Xiao, W. He, P. Subasic, A. R. Harutyunyan, Y. Wang, F. Liu, H. Xu and J. Li, Approaching coupled-cluster accuracy for molecular electronic structures with multi-task learning, *Nat. Comput. Sci.*, 2024, **5**, 1–11.
36 B. Das and A. Mondal, Predictive Modeling and Design of Organic Solar Cells: A Data-Driven Approach for Material Innovation, *ACS Appl. Energy Mater.*, 2024, **7**, 9349–9363.
37 H. Sahu, W. Rao, A. Troisi and H. Ma, Toward predicting efficiency of organic solar cells via machine learning and improved descriptors, *Adv. Energy Mater.*, 2018, **8**, 1801032.
38 R. Ouyang, S. Curtarolo, E. Ahmetcik, M. Scheffler and L. M. Ghiringhelli, SISSO: A compressed-sensing method for identifying the best low-dimensional descriptor in an immensity of offered candidates, *Phys. Rev. Mater.*, 2018, **2**, 083802.
39 R. Ouyang, E. Ahmetcik, C. Carbogno, M. Scheffler and L. M. Ghiringhelli, Simultaneous learning of several materials properties from incomplete databases with multi-task SISSO, *JPhys Mater.*, 2019, **2**, 024002.
40 R. Pariser and R. G. Parr, A Semi-Empirical Theory of the Electronic Spectra and Electronic Structure of Complex Unsaturated Molecules. I, *J. Chem. Phys.*, 1953, **21**, 466–471.
41 R. Pariser and R. G. Parr, A Semi-Empirical Theory of the Electronic Spectra and Electronic Structure of Complex Unsaturated Molecules. II, *J. Chem. Phys.*, 1953, **21**, 767–776.
42 J. A. Pople, Electron interaction in unsaturated hydrocarbons, *Trans. Faraday Soc.*, 1953, **49**, 1375–1385.
43 Sanyam, R. Khatua and A. Mondal, Cost-Effective Approach for Modeling of Multiresonant Thermally Activated Delayed Fluorescence Emitters, *J. Chem. Theory Comput.*, 2023, **19**, 9290–9301.
44 W. Cai, C. Zhong, Z.-W. Ma, Z.-Y. Cai, Y. Qiu, Z. Sajid and D.-Y. Wu, Machine-learning-assisted performance improvements for multi-resonance thermally activated delayed fluorescence molecules, *Phys. Chem. Chem. Phys.*, 2024, **26**, 144–152.
45 Z. Tan, Y. Li, Z. Zhang, T. Penfold, W. Shi, S. Yang and W. Zhang, A deep learning framework for predictions of excited state properties of light emissive molecules, *New J. Chem.*, 2023, **47**, 9550–9554.
46 C. Tu, W. Huang, S. Liang, K. Wang, Q. Tian and W. Yan, Combining machine learning and quantum chemical calculations for high-throughput virtual screening of thermally activated delayed fluorescence molecular materials: the impact of selection strategy and structural mutations, *RSC Adv.*, 2022, **12**, 30962–30975.
47 T. Akiba, S. Sano, T. Yanase, T. Ohta and M. Koyama, Optuna: A next-generation hyperparameter optimization framework, *Proceedings of the 25th ACM SIGKDD International Conference on Knowledge Discovery & Data Mining*, 2019, pp. 2623–2631.
48 T. Hatakeyama, K. Shiren, K. Nakajima, S. Nomura, S. Nakatsuka, K. Kinoshita, J. Ni, Y. Ono and T. Ikuta, Ultrapure blue thermally activated delayed fluorescence molecules: efficient HOMO–LUMO separation by the multiple resonance effect, *Adv. Mater.*, 2016, **28**, 2777–2781.
49 K. Matsui, S. Oda, K. Yoshiura, K. Nakajima, N. Yasuda and T. Hatakeyama, One-shot multiple borylation toward BN-doped nanographenes, *J. Am. Chem. Soc.*, 2018, **140**, 1195–1198.
50 S. Oda, B. Kawakami, R. Kawasumi, R. Okita and T. Hatakeyama, Multiple resonance effect-induced sky-blue thermally activated delayed fluorescence with a narrow emission band, *Org. Lett.*, 2019, **21**, 9311–9314.
51 Y. Yuan, X. Tang, X.-Y. Du, Y. Hu, Y.-J. Yu, Z.-Q. Jiang, L.-S. Liao and S.-T. Lee, The design of fused amine/carbonyl system for efficient thermally activated delayed

fluorescence: novel multiple resonance core and electron acceptor, *Adv. Opt. Mater.*, 2019, **7**, 1801536.

52 X. Wu, J.-W. Huang, B.-K. Su, S. Wang, L. Yuan, W.-Q. Zheng, H. Zhang, Y.-X. Zheng, W. Zhu and P.-T. Chou, Fabrication of Circularly Polarized MR-TADF Emitters with Asymmetrical Peripheral-Lock Enhancing Helical B/N-Doped Nanographenes, *Adv. Mater.*, 2022, **34**, 2105080.

53 J. A. Knöller, G. Meng, X. Wang, D. Hall, A. Pershin, D. Beljonne, Y. Olivier, S. Laschat, E. Zysman-Colman and S. Wang, Intramolecular borylation via sequential B- Mes bond cleavage for the divergent synthesis of B, N, B-doped benzo [4] helicenes, *Angew. Chem., Int. Ed.*, 2020, **59**, 3156–3160.

54 R. K. Konidena and K. R. Naveen, Boron-Based Narrowband Multiresonance Delayed Fluorescent Emitters for Organic Light-Emitting Diodes, *Adv. Photonics Res.*, 2022, **3**, 2200201.

55 H. Hirai, K. Nakajima, S. Nakatsuka, K. Shiren, J. Ni, S. Nomura, T. Ikuta and T. Hatakeyama, One-step borylation of 1, 3-diaryloxybenzenes towards efficient materials for organic light-emitting diodes, *Angew. Chem.*, 2015, **127**, 13785–13789.

56 Y. Xu, Z. Cheng, Z. Li, B. Liang, J. Wang, J. Wei, Z. Zhang and Y. Wang, Molecular-structure and device-configuration optimizations toward highly efficient green electroluminescence with narrowband emission and high color purity, *Adv. Opt. Mater.*, 2020, **8**, 1902142.

57 X. Xiong, Y.-C. Cheng, K. Wang, J. Yu and X.-H. Zhang, A comparative study of two multi-resonance TADF analogous materials integrating chalcogen atoms of different periods, *Mater. Chem. Front.*, 2023, **7**, 929–936.

58 N. Ikeda, S. Oda, R. Matsumoto, M. Yoshioka, D. Fukushima, K. Yoshiura, N. Yasuda and T. Hatakeyama, Solution-processable pure green thermally activated delayed fluorescence emitter based on the multiple resonance effect, *Adv. Mater.*, 2020, **32**, 2004072.

59 M. Nagata, H. Min, E. Watanabe, H. Fukumoto, Y. Mizuhata, N. Tokitoh, T. Agou and T. Yasuda, Fused-Nonacyclic Multi-Resonance Delayed Fluorescence Emitter Based on Ladder-Thiaborin Exhibiting Narrowband Sky-Blue Emission with Accelerated Reverse Intersystem Crossing, *Angew. Chem.*, 2021, **133**, 20442–20447.

60 I. S. Park, H. Min and T. Yasuda, Ultrafast Triplet–Singlet Exciton Interconversion in Narrowband Blue Organoboron Emitters Doped with Heavy Chalcogens, *Angew. Chem., Int. Ed.*, 2022, **61**, e202205684.

61 F. Neese, The ORCA program system, *Wiley Interdiscip. Rev.: Comput. Mol. Sci.*, 2012, **2**, 73–78.

62 K. T. Schutt, P.-J. Kindermans, H. E. Sauceda, S. Chmiela, A. Tkatchenko and K.-R. Muller, SchNet: a continuous-filter convolutional neural network for modelingquantum interactions, *Proceedings of the 31st International Conference on Neural Information Processing Systems*, Red Hook, NY, USA, 2017, pp. 992–1002.

